

2019-08

Magnetic inflation and stellar mass. III. revised parameters for the component stars of NSVS 07394765






Brian F. Healy, Eunkyun Han, Philip S. Muirhead, Brian Skiff, Tom Polakis, Anneliese Riling, Jonathan J. Swift. 2019. "Magnetic Inflation and Stellar Mass. III. Revised Parameters for the Component Stars of NSVS 07394765." *The Astronomical Journal*, Volume 158, Issue 2, pp. 89 - 89. <https://doi.org/10.3847/1538-3881/ab2fe5>

<https://hdl.handle.net/2144/39802>

"Downloaded from OpenBU. Boston University's institutional repository."



Magnetic Inflation and Stellar Mass. III. Revised Parameters for the Component Stars of NSVS 07394765

Brian F. Healy^{1,2} , Eunkyu Han² , Philip S. Muirhead² , Brian Skiff³, Tom Polakis⁴, Anneliese Rilinger² , and Jonathan J. Swift⁵ 

¹Department of Physics and Astronomy, Johns Hopkins University, 3400 North Charles Street, Baltimore, MD 21218, USA; bfhealy@jhu.edu

²Department of Astronomy & Institute for Astrophysical Research, Boston University, 725 Commonwealth Avenue, Boston, MA 02215, USA

³Lowell Observatory, 1400 West Mars Hill Road, Flagstaff, AZ 86001, USA

⁴Command Module Observatory, 121 West Alameda Drive, Tempe, AZ 85282, USA

⁵The Thacher School, 5025 Thacher Road, Ojai, CA 93023, USA

Received 2018 December 7; revised 2019 July 4; accepted 2019 July 5; published 2019 July 31

Abstract

We perform a new analysis of the M-dwarf–M-dwarf eclipsing binary system NSVS 07394765 in order to investigate the reported hyper-inflated radius of one of the component stars. Our analysis is based on archival photometry from the Wide Angle Search for Planets, new photometry from the 32 cm Command Module Observatory telescope in Arizona and the 70 cm telescope at Thacher Observatory in California, and new high-resolution infrared spectra obtained with the Immersion Grating Infrared Spectrograph on the Discovery Channel Telescope. The masses and radii we measure for each component star disagree with previously reported measurements. We show that both stars are early M-type main-sequence stars without evidence for youth or hyper-inflation ($M_1 = 0.661_{-0.036}^{+0.008} M_\odot$, $M_2 = 0.608_{-0.028}^{+0.003} M_\odot$, $R_1 = 0.599_{-0.019}^{+0.032} R_\odot$, $R_2 = 0.625_{-0.027}^{+0.012} R_\odot$), and we update the orbital period and eclipse ephemerides for the system. We suggest that the likely cause of the initial hyper-inflated result is the use of moderate-resolution spectroscopy for precise radial velocity measurements.

Key words: binaries: close – binaries: eclipsing – binaries: spectroscopic – stars: fundamental parameters – stars: individual (NSVS 07394765) – stars: late-type

Supporting material: data behind figures

1. Introduction

The faintest and coolest stars in the Milky Way make up for their dimness with their sheer number: over 70% of the stars in the galaxy are main-sequence M-dwarf stars (e.g., Chabrier 2005). These stars typically have a temperature range of 2300–3800 K, a mass range of ~ 0.075 – $0.60 M_\odot$, and a radius range of 0.08 – $0.62 R_\odot$. Since the maximum luminosity of an M dwarf is less than 10% that of the Sun, it can be difficult to investigate their properties, especially when they are isolated. When their presence is observed within a detached, noninteracting eclipsing binary (EB), however, the opportunity to learn about both stars in the system greatly increases.

Previous studies of M dwarfs in detached EBs have shown an empirical relationship between the mass and radius of these stars (Torres et al. 2010). The empirical relationship appears to show larger radii for a given mass than predictions from evolutionary models (e.g., Feiden & Chaboyer 2013), and the individual M dwarfs show significant scatter around this relationship (Parsons et al. 2018). One potential explanation for the inflated M dwarfs involves effects from magnetic fields. In magnetically active stars, strong magnetic fields may disrupt stellar convection cells that transport energy toward the surface. The effect can be simulated using mixing length theory by increasing the mixing length parameter in stellar evolutionary models (Chabrier et al. 2007).

In this scenario, the lowered convective efficiency leads to a steeper temperature gradient, resulting in a lower stellar effective temperature, T_{eff} . Since the star’s nuclear reaction rate and corresponding luminosity are nearly unchanged, a lower T_{eff} leads to a higher inflated radius compared to a star

with higher convective efficiency. Recent work by MacDonald & Mullan (2017) suggests that the observed inflation can be caused by magnetic fields less than 10 kG. However, even in the most magnetically active M dwarfs, this process is not expected to inflate stellar radii beyond around 25% of their noninflated counterparts, and only for M dwarfs that are partially convective. For fully convective M dwarfs, a different mechanism involving starspots may cause inflation through flux suppression (Chabrier et al. 2007). In a recent paper in this series, Kesseli et al. (2018) showed that single, rapidly rotating, fully convective stars also appear larger than evolutionary models predict, providing evidence for flux suppression by magnetized starspots.

Challenging these proposed scenarios are several main-sequence EBs that appear to be hyper-inflated, with radii far greater than either the empirical trend or model predictions for their masses, even after considering the effects of strong magnetic fields. One example is T-Cyg1-12664, a main-sequence low-mass EB with *Kepler* photometry, which initially appeared to contain hyper-inflated components (Cakırlı et al. 2013; Iglesias-Marzoa et al. 2017). In a previous paper as part of this series, Han et al. (2017) showed that neither component star of T-Cyg1-12664 showed evidence of hyper-inflation, and that both are consistent with the empirical mass–radius trend seen in typical EBs. They attributed the discrepancy to the use of high-resolution near-infrared spectroscopy, which provided higher-fidelity radial velocity observations of both component stars.

Another hyper-inflated detached EB, NSVS 07394765 (hereafter NSVS 0739), is reported to have an M-dwarf component with a radius and mass of $0.50 R_\odot$ and $0.18 M_\odot$, respectively (Cakırlı, 2013). This radius is more than twice the

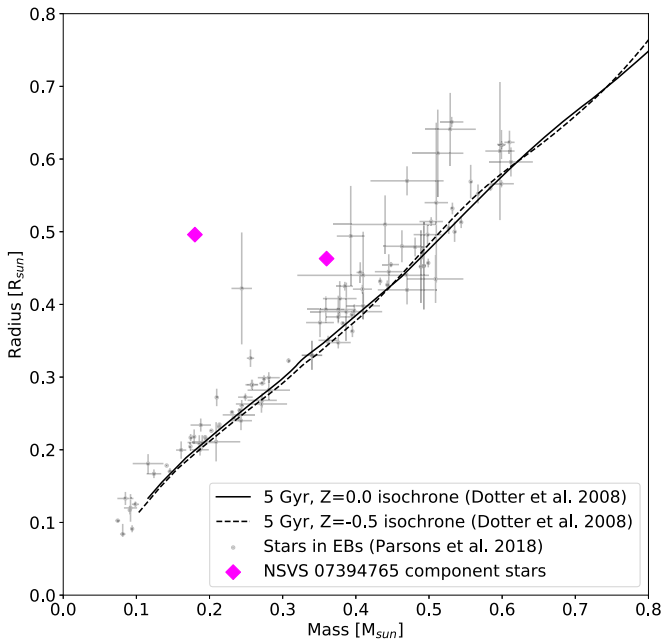


Figure 1. Mass–radius plot of Dartmouth 5 Gyr stellar isochrones (Dotter et al. 2008) for metallicities of 0.0 and -0.5 dex and stars in detached eclipsing binaries with reliable measurements from the literature (see Parsons et al. 2018, their Table A1). The reported measurements of the components of NSVS 0739 are shown in magenta, with reported uncertainties that are smaller than the size of the points. There is a discrepancy greater than 20σ between the models and the reported masses and radii.

predictions from either stellar evolutionary models (Dotter et al. 2008) or empirical trends (Figure 1), deviating significantly even from predictions involving magnetic inflation. The other M dwarf in this system is reported to be less inflated, with parameters of $0.46 R_{\odot}$ and $0.36 M_{\odot}$.

These parameters suggest that NSVS 0739 is an ideal system for testing theories of stellar inflation. For an M dwarf to be this inflated, it must be either a nascent star that is in the process of contracting (pre-main-sequence), or the result of some unknown mechanism. If it is young, the star would offer valuable information about the evolutionary track of M dwarfs (e.g., Kraus et al. 2015; Gillen et al. 2017).

Thus, we investigated NSVS 0739 to determine if one of the components is in fact a pre-main-sequence star. In our examination of this system, we found that neither M-dwarf component of NSVS 0739 is hyper-inflated or even moderately inflated compared to the mass–radius trend (see Section 3.2). Instead, the revised parameters are in statistical compatibility with the empirical mass–radius relation. We argue, similar to Han et al. (2017), that our use of high-resolution infrared spectroscopy to measure radial velocities improved the accuracy of those measurements.

In Section 2 of this paper, we describe our photometric and spectroscopic data and the reduction of these data. In Section 3, we present the results from fitting an EB model to the data, using the same procedure outlined in Han et al. (2017). Section 4 discusses discrepancies between our results and published values, and Section 5 states our conclusions from this work.

2. Data and Reduction

2.1. Archival Photometry

We accessed the NASA Exoplanet Archive (Akeson et al. 2013) to download publicly available data for NSVS 0739 from

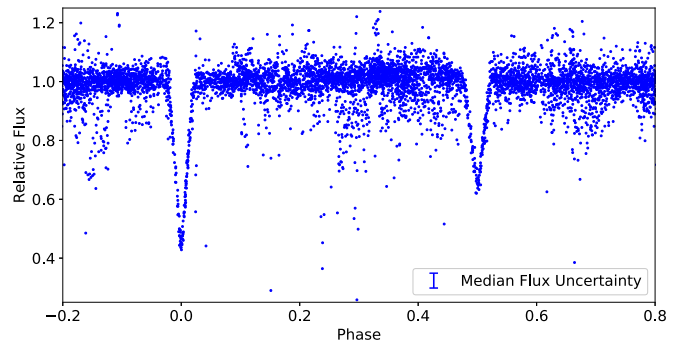


Figure 2. Phase-folded WASP light curve for NSVS 0739. The data have been cleaned of erroneous in-eclipse data points. The legend shows the median flux uncertainty.

Table 1
Description of WASP Observations for NSVS 0739

Coordinates (R.A. Decl.)	$8^{\text{h}}25^{\text{m}}51^{\text{s}}.894$, $24^{\circ}27'4''60$
WASP magnitude	13.17819
Start time (BJD)	2453261.742889
End time (BJD)	2454575.437458
Number of points	6718

the Wide Angle Search for Planets (WASP; Butters et al. 2010). The WASP passband ranges from ~ 400 – 700 nm, roughly encompassing the Sloan g and r bands. The observations were made between 2004 September and 2008 April for a total of 6718 photometric data points. With a V -band magnitude of 13.0, NSVS 0739 is near the limiting magnitude of the survey, introducing noticeable noise into the light curve. Nonetheless, Figure 2 shows that WASP clearly detected both eclipses for the system. See Table 1 for the details of the WASP observations.

We removed two nights of WASP data for which there were data points significantly deviating from the expected in-eclipse value despite having a phase corresponding to an eclipse. These points were likely caused by adverse weather conditions during these nights. We also established a maximum relative flux limit of 1.1 to exclude extreme increases in flux corresponding to weather or flares on the component stars. We converted time units from the archive-supplied HJD to BJD_{TDB} using a calculator by Eastman et al. (2010).

2.2. New Photometry

We also obtained a new NSVS 0739 primary eclipse observation on UT 2017 February 1 using the 32 cm Dall-Kirkham telescope at CMO in Tempe, AZ. The detector is a thermo-electrically cooled SBIG ST-6303On CCD. The night was photometric, and we acquired 180-second exposures in the Johnson V band. We used the commercial software package MPO Canopus to perform aperture photometry on NSVS 0739 and four reference stars with $15''$ apertures and sky annulus subtraction. This software specializes in asteroid and variable star analyses, offering a graphical interface for image calibration, astrometry, and photometry. We used the AAVSO Photometric All-Sky Survey (APASS) DR9 to supply V magnitudes for the reference stars. Because we observed multiple targets on this night, there are gaps in coverage of the NSVS 0739 eclipse (Figure 3).

We observed another primary eclipse (Figure 4) on UT 2019 April 14 with the 0.7 m telescope at Thacher Observatory in

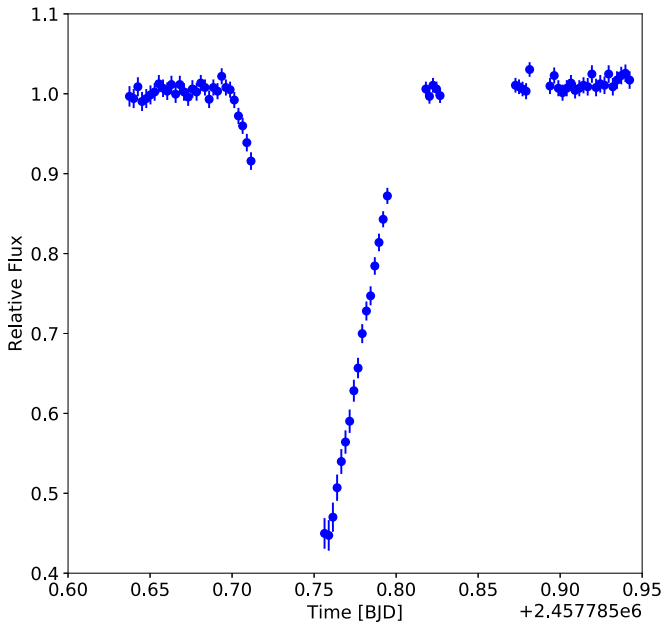


Figure 3. Additional V-band primary eclipse light curve observed at the Command Module Observatory on UT 2017 February 1.

(The data used to create this figure are available).

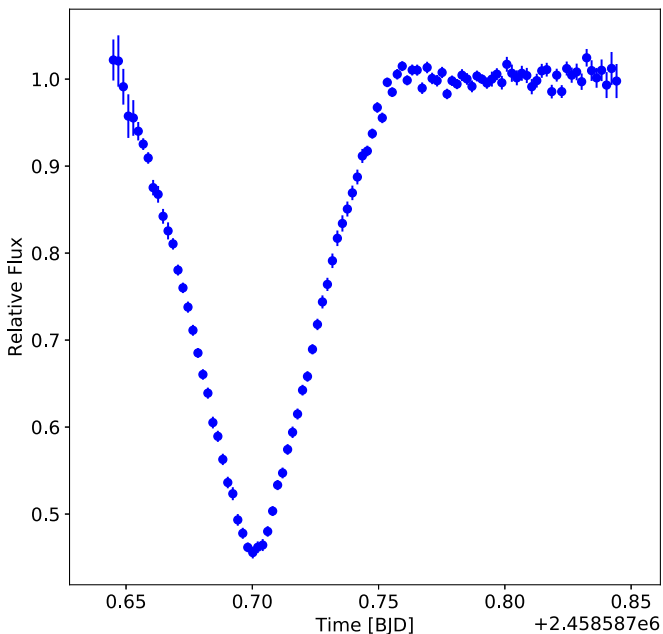


Figure 4. Additional V-band primary eclipse light curve observed at the Thacher Observatory on UT 2019 April 14.

(The data used to create this figure are available).

Ojai, CA (O’Neill et al. 2017; Swift & Vyhna 2018). The new observation was made in the Johnson V band with integration times of 1 minute. We reduced the data using the *astropy* utilities in Python (Astropy Collaboration et al. 2013, 2018). We performed aperture photometry on NSVS 0739 and two nearby reference stars that we tested for stability and high S/N. Given the variability of the seeing, we optimized the aperture used in each image to maximize the S/N on NSVS 0739, and

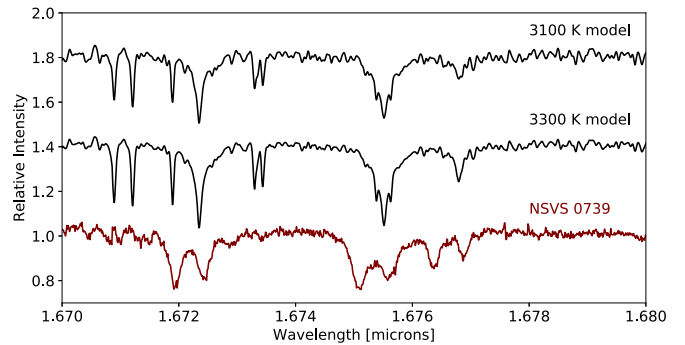


Figure 5. Example IGRINS tenth-order *H*-band spectrum for NSVS 0739 (maroon), observed on UT 2016 November 10. The double-lined nature of this binary system is apparent in the duplication of an AII triplet in this order (Cushing et al. 2005). Two BT-Settl model spectra, representing stars with 3100 and 3300 K effective temperatures, are plotted above with a vertical offset.

we chose sky radii from stacked images to avoid background sources in areas outside the wings of the point-spread function (PSF). The final light curve was stable and did not require us to fit the out-of-eclipse data for a trend in airmass or time.

2.3. Spectroscopy

We used the Immersion Grating Infrared Spectrograph (IGRINS; Park et al. 2014; Prato 2017) at the Discovery Channel Telescope to obtain spectra for NSVS 0739 at five different times. IGRINS is a cross-dispersed, near-infrared, high-resolution spectrometer covering wavelengths between 1.45 and 2.45 μm (*H* and *K* bands) at $R \sim 45,000$. Calculated exposure times were intended to provide an S/N of at least 10. See Figure 5 for an example *H*-band spectrum. Given that the orbital period of NSVS 0739 was on the order of two days, useful observations only needed to be separated by a few hours.

We reduced the IGRINS data following the procedures described in Han et al. (2017). Briefly, the first step involved feeding the raw data through the IGRINS pipeline (Sim et al. 2014). We then used observations of a nearby A0 star to calibrate for telluric lines. We observed the A0 star on the same night as each target observation, under similar weather conditions. The telluric correction was done using the `xtellcor_general` data reduction software package written in IDL (Vacca et al. 2003). The software propagates uncertainties in the telluric correction to the final uncertainties in the spectra.

Using TODCOR (Zucker & Mazeh 1994), we performed a two-dimensional cross-correlation between two template BT-Settl model spectra (Allard et al. 2012; Baraffe et al. 2015) for stars with 3100 and 3300 K effective temperatures (Figure 5) and high-S/N spectral orders 8–14 of our *H*-band IGRINS data to find the radial velocity of both stars in the system (e.g., Figure 6). Orders near the edges of the detector experience distortions that diminish the quality of the derived radial velocities, and other unused orders contain large telluric features that are not sufficiently corrected by the A0 calibration spectrum. We obtained uncertainties on the radial velocities by performing cross-correlation with each order independently and taking a standard deviation of the mean of the results. We did not use the lower-S/N *K*-band data from IGRINS because the cross-correlation functions were not as definitive in this band. To account for the motion of the Earth around the Sun, we

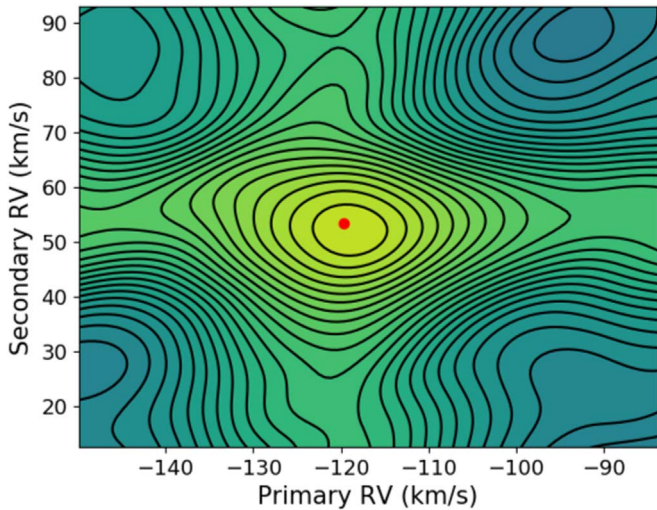


Figure 6. Example two-dimensional cross-correlation of template and target spectra with TODCOR (Zucker & Mazeh 1994) to obtain primary and secondary radial velocities.

Table 2

New Barycenter-corrected NSVS 0739 Radial Velocities Calculated from IGRINS *H*-band Spectra

Band (1)	Time (BJD _{TDB}) (2)	Phase (3)	Primary RV (km s ⁻¹) (4)	Secondary RV (km s ⁻¹) (5)
<i>H</i>	2457702.86978	0.411	-48.2 ± 2.5	43.2 ± 2.5
<i>H</i>	2457702.94347	0.444	-31.4 ± 2.6	27.8 ± 1.2
<i>H</i>	2458022.00737	0.287	-84.8 ± 1.2	84.8 ± 4.8
<i>H</i>	2458023.02147	0.735	80.1 ± 1.1	-94.3 ± 3.6
<i>H</i>	2458473.95167	0.788	76.9 ± 6.4	-94.5 ± 11.2

performed a barycentric correction using the tools of Wright & Eastman (2014). Table 2 lists the five new radial velocity points.

3. Analysis and Results

3.1. Model Fitting

Under the assumption that the passbands of WASP, the Command Module Observatory (CMO), and Thacher data overlapped, we fit a model to the photometry and radial velocities based on the *eb* software by Irwin et al. (2011). This code generates simulated photometry and radial velocity curves. The upper rows of Table 3 show the model parameters that were fitted. Under the assumption of no third light, and neglecting the effect of light-travel time due to the system’s nearly equal-mass components and low eccentricity, we made an initial least-squares fit using *mpfit* (Markwardt 2009). Initiating uniform priors for each parameter centered on our results from *mpfit*, we performed a Markov chain Monte Carlo (MCMC) exploration of parameter space using *emcee* (Foreman-Mackey et al. 2013). For the MCMC, we established a normal likelihood function (LF) of the form

$$\ln(\text{LF}) = -0.5 * \sum_{i=1}^{n_{\text{points}}} \left[\frac{(y_i - \hat{y}_i)^2}{\sigma_i^2} + \ln(2\pi\sigma_i^2) \right], \quad (1)$$

summing over all points (n_{points}) in the phase-folded data (y_i) in comparison with model points (\hat{y}_i) generated by *eb* and the

uncertainty of each data point, σ_i . For each step out of the total 50,000 and each chain out of 100, we performed Affine-Invariant sampling of the fitted parameters with the EnsembleSampler class of *emcee*. After visual inspection of the chains for each parameter, we discarded a burn-in of the first 10,000 steps to prevent our results from being biased toward the prior values.

Due to the small number of radial velocity data points compared to the plentiful photometric points, we performed the latter fit separately from the former, with the same number of steps, chains, and burn-in. This separation of fits ensured that the overall determination of goodness-of-fit was not dominated only by photometry (see Section 3.2 of Han et al. 2017, who also used this fitting method). We show the final photometric fit (including WASP, CMO, and Thacher eclipses) and residuals in Figure 7. The residual structure visible in the CMO and Thacher primary eclipse fits shows the limitation of the assumption that the WASP passband overlaps with these *V*-band observations. Nonetheless, these new data helped to better constrain the period and time of mid-primary eclipse by roughly quadrupling the time baseline of eclipse observations and supplementing WASP data with higher-cadence coverage. The primary and secondary radial velocity fits appear in Figure 8.

We fit limb-darkening coefficients for each star using the square-root model demonstrated to be effective for low-mass M dwarfs in Claret (1998). During fitting, we parameterized limb-darkening in terms of q_1 and q_2 from Kipping (2013). Though the final fit did not provide strong constraints on these coefficients, the sampling of a wide variety of limb-darkening coefficients induced additional variation in the best-fit parameters for each step, widening the distribution of the calculated radius values compared to a fit with better-constrained limb-darkening coefficients. Therefore, limb-darkening uncertainties are incorporated into the error of the other fitted parameters.

3.2. Results

The MCMC run yielded 100 chains of 40,000 values for every fitted parameter (after discarding the burn-in steps). To solve for the desired results and their uncertainties, we calculated each final parameter from its distribution of all 4×10^6 values. We adopted each distribution’s maximum-likelihood value to be the reported parameter value and computed its difference from the 16th and 84th percentiles of each distribution to establish the 1σ confidence intervals reported as our uncertainties. For the eccentricity parameter, we instead used the 0th and 68th percentiles for error bars, because the nearly circular system does not have a normal distribution about the highest-likelihood value. Table 3 lists the maximum-likelihood fitted and calculated parameters with their 1σ uncertainties. Note that to minimize the results’ dependence on stellar atmospheric models, we do not compute the stellar effective temperature or luminosity ratio. See Section 4.5 of Han et al. (2017) for a further explanation. We show triangle plots (Foreman-Mackey 2016) for the photometric and radial velocity fits in Figures 9 and 10, respectively. We note that our ephemeris predicts future eclipses at significantly different times than the discovery papers.

After our analysis, the stars now fall into statistical agreement with the empirical and theoretical mass–radius trends for M dwarfs (Figure 11). We discuss our confidence in

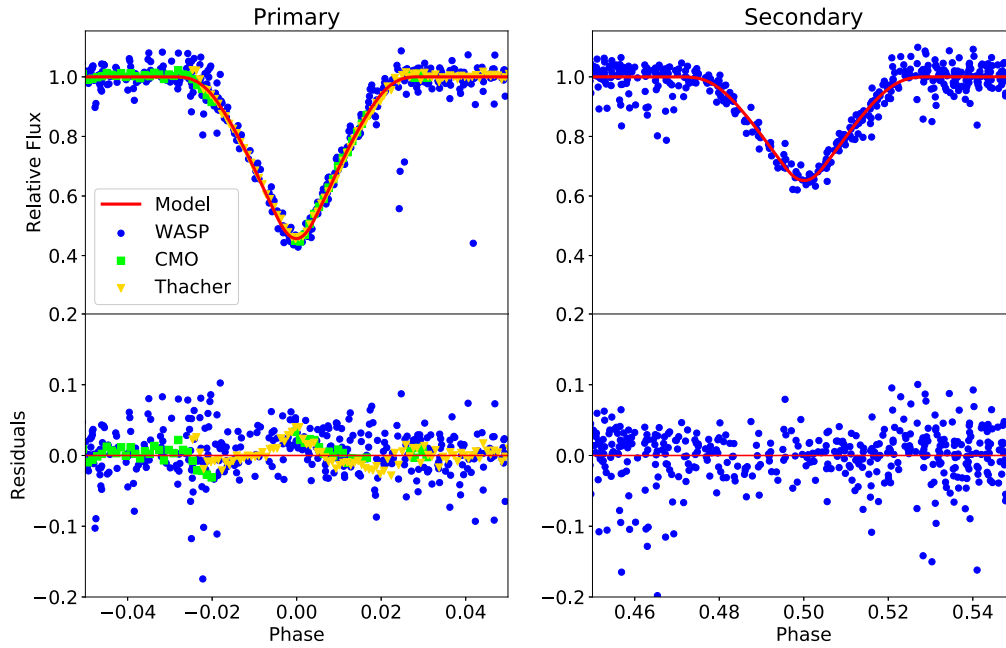


Figure 7. Model fit and residuals for WASP, CMO, and Thacher primary and secondary eclipses. The shape of the CMO and Thacher residuals illustrates the difference between the WASP and V passbands.

Table 3
NSVS 0739 Fitted and Calculated Parameter Descriptions, Maximum-likelihood Values, and 1σ Uncertainties

Fitted Parameter (1)	Description (2)	NSVS 07394765 (3)
J	Central surface brightness ratio	$0.66^{+0.20}_{-0.06}$
$(R_1 + R_2)/a$	Fractional radii sum over semimajor axis	$0.1555^{+0.0022}_{-0.0006}$
R_2/R_1	Radius ratio	$1.043^{+0.053}_{-0.093}$
$\cos i$	Cosine of orbital inclination	$0.0041^{+0.0020}_{-0.0036}$
P	Orbital period	$2.26537743^{+0.00000021}_{-0.00000005}$ days
T_0	Time of primary mid-eclipse	$2454573.45195^{+0.00011}_{-0.00029}$ BJD _{TDB}
$e \cos \omega$	Eccentricity \times cosine of argument of periastron	$-0.00011^{+0.00035}_{-0.00020}$
$e \sin \omega$	Eccentricity \times sine of argument of periastron	$-0.001^{+0.027}_{-0.010}$
γ	Center of mass system velocity	$-3.5^{+0.5}_{-1.3}$ km s ⁻¹
q	Mass ratio (M_2/M_1)	$0.921^{+0.017}_{-0.014}$
K_{tot}/c	Sum of radial velocity semi-amplitudes/speed of light	$0.0005860^{+0.0000015}_{-0.0000096}$
u_{11}	Linear limb-darkening coefficient, star 1	$-0.22^{+0.60}_{-0.54}$
u_{21}	Square-root limb-darkening coefficient, star 1	$0.43^{+0.45}_{-0.87}$
u_{12}	Linear limb-darkening coefficient, star 2	$0.9^{+0.7}_{-1.4}$
u_{22}	Square-root limb-darkening coefficient, star 2	$0.1^{+1.0}_{-0.6}$
Calculated Parameter	Description	NSVS 07394765
e	Eccentricity	$0.001^{+0.017}_{-0.001}$
i	Orbital inclination	$89.76^{+0.21}_{-0.12}$ degrees
a	Semimajor axis	$0.03651^{+0.00009}_{-0.00060}$ au
K_1	Radial velocity semi-amplitude, star 1	$84.3^{+0.2}_{-1.3}$ km s ⁻¹
K_2	Radial velocity semi-amplitude, star 2	$91.5^{+0.7}_{-2.1}$ km s ⁻¹
M_1	Mass, star 1	$0.661^{+0.008}_{-0.036} M_{\odot}$
M_2	Mass, star 2	$0.608^{+0.003}_{-0.028} M_{\odot}$
R_1	Radius, star 1	$0.599^{+0.032}_{-0.019} R_{\odot}$
R_2	Radius, star 2	$0.625^{+0.012}_{-0.027} R_{\odot}$
$\log g_1$	Log of surface gravity, star 1 (cgs)	$4.705^{+0.018}_{-0.051}$
$\log g_2$	Log of surface gravity, star 2 (cgs)	$4.632^{+0.028}_{-0.024}$
L_2/L_1	Orbit-averaged photometric light ratio	$0.72^{+0.31}_{-0.18}$

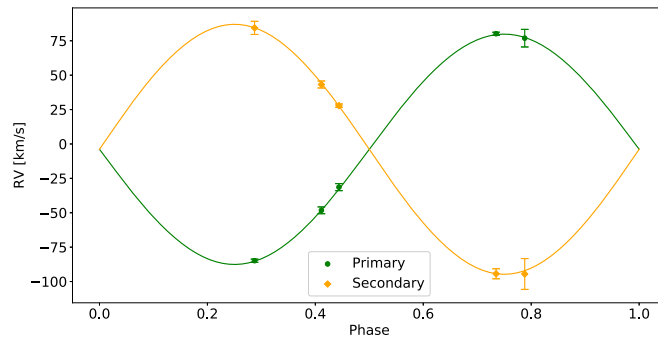


Figure 8. Radial velocity fit to the five IGRINS data points.

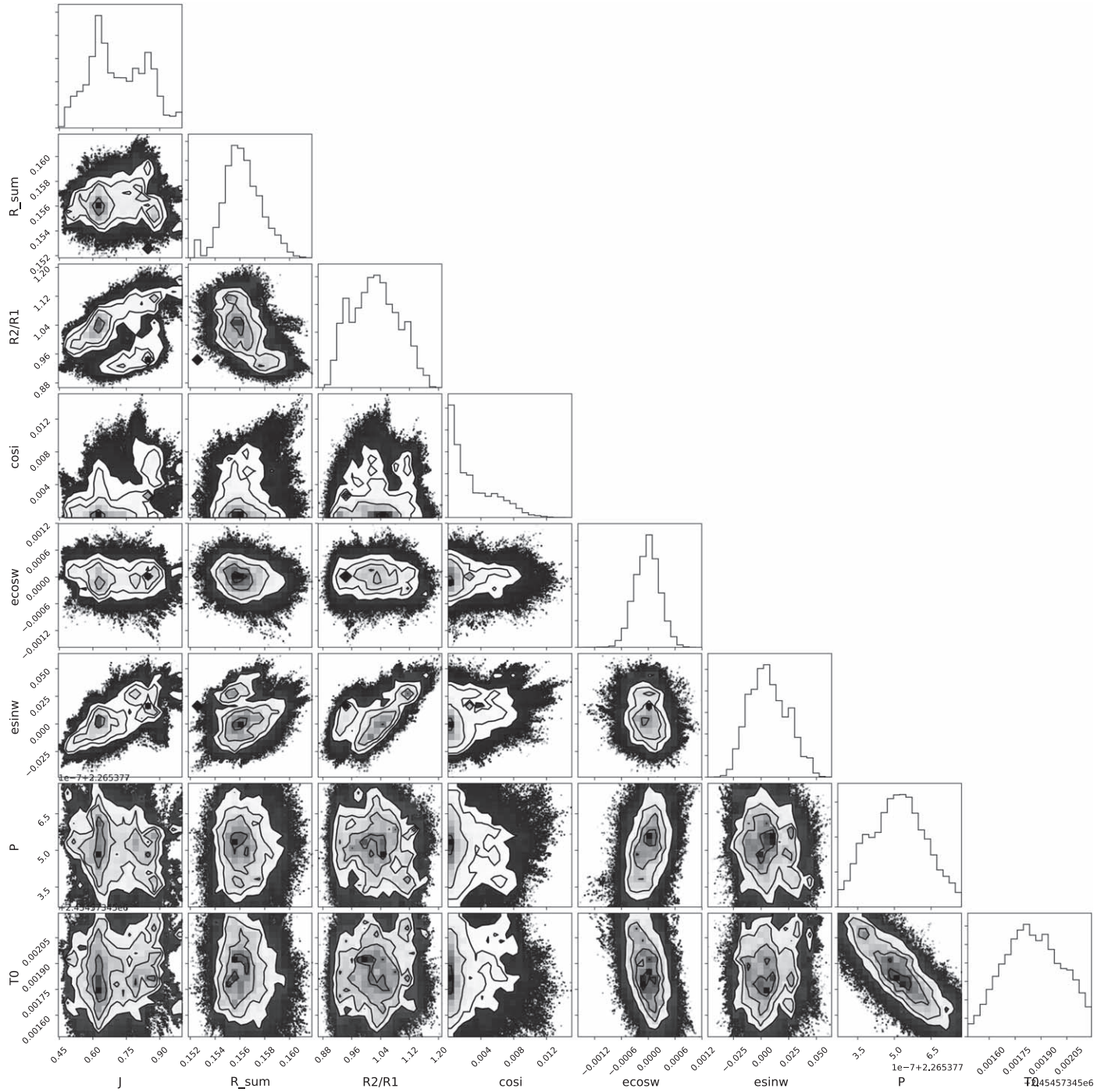


Figure 9. Triangle plot of fitted NSVS 0739 light curve parameters.

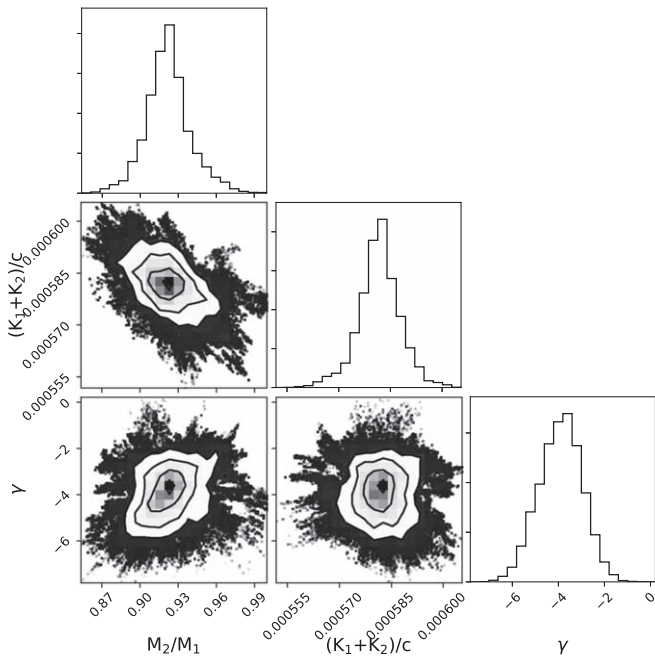


Figure 10. Triangle plot of fitted NSVS 0739 RV parameters.

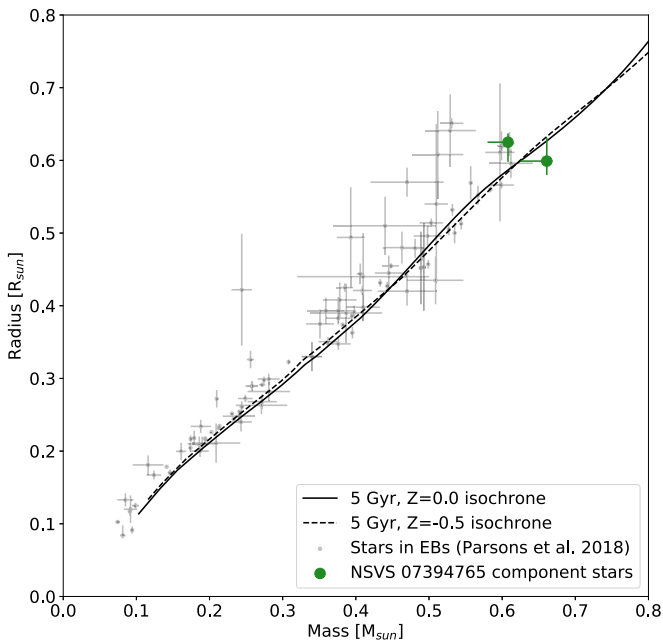


Figure 11. Mass–radius plot of theoretical 5 Gyr isochrones, stars in eclipsing binaries from Parsons et al. (2018), and our revised parameters for NSVS 0739 and their uncertainties.

the new masses and radii, along with a possible cause for the initial hyper-inflated results, in Section 4.

4. Discussion

Our analysis supports a different argument than previous work: that (1) the NSVS 0739 M dwarfs are larger and more massive than their initial published values, (2) they are nearly equal mass, and (3) they are not inflated.

Our calculated primary radial velocity semi-amplitude of $84.3^{+0.2}_{-1.3}$ km s⁻¹ differs greatly from the previous work’s value of 44 ± 3 km s⁻¹. This large disagreement between the two

works likely accounts for the majority of the discrepancy in mass and radius results. A possible cause for the hyper-inflated results in the previous paper may be the use of lower-resolution ($\frac{\lambda}{\Delta\lambda} = 7000$ compared to $\sim 45,000$ for IGRINS) spectral observations.

Spectral line blending can make cross-correlation with a model spectrum more difficult, and such an analysis may bias the derived radial velocities. The dramatically different solution to the system using our high-resolution IGRINS radial velocities supports this hypothesis.

5. Conclusion

Undertaking a new analysis of the EB system NSVS 07394765 revealed radial velocity measurements in discrepancy with previous work. It is likely that our high-resolution spectroscopy allowed for a more unbiased determination of radial velocities than was possible with the previous work’s moderate-resolution observations. The uniformity in our primary and secondary radial velocity amplitudes suggests that the stellar mass ratio is near one-to-one. Moreover, these observations support a system that does not contain inflated M dwarfs.

We conclude that neither M dwarf in NSVS 07394765 is hyper-inflated. We also conclude that the system has a larger total mass that is nearly equally divided among its two components, which are likely early M dwarfs or late K dwarfs. Our results should be considered preliminary, as the characterization of this system would still benefit from further photometric and spectroscopic observations. This work underscores the importance of high-resolution infrared spectroscopy in the further study of low-mass stars in eclipsing binaries. As the field of astronomy moves closer to a comprehensive mass–radius–luminosity relation for M dwarfs, our results will be an important contribution to constraining these connections.

We thank the anonymous referee for helpful comments and critique. B.F.H. thanks Ömür Çakırlı for helpful correspondence. P.S.M. acknowledges support from the NASA Exoplanet Research Program (XRP) under grant No. NNX15AG08G issued through the Science Mission Directorate. This research involved use of the Discovery Channel Telescope at Lowell Observatory, supported by Discovery Communications, Inc., Boston University, the University of Maryland, the University of Toledo, Northern Arizona University and Yale University. This research involved use of the Immersion Grating Infrared Spectrometer (IGRINS) that was developed under a collaboration between the University of Texas at Austin and the Korea Astronomy and Space Science Institute (KASI) with the financial support of the US National Science Foundation under grant AST-1229522, of the University of Texas at Austin, and of the Korean GMT Project of KASI. This research has made use of the APASS database, located at the AAVSO website. Funding for APASS has been provided by the Robert Martin Ayers Sciences Fund.

Facilities: DCT (IGRINS), WASP.

Software: *astropy* (Astropy Collaboration et al. 2013, 2018), *eb* (Irwin et al. 2011), *emcee* (Foreman-Mackey et al. 2013), *mpfit* (Markwardt 2009), *TODCOR* (Zucker & Mazeh 1994), *xtellcor* (Vacca et al. 2003).

ORCID iDs

Brian F. Healy  <https://orcid.org/0000-0002-7718-7884>
 Eunkyu Han  <https://orcid.org/0000-0001-9797-0019>
 Philip S. Muirhead  <https://orcid.org/0000-0002-0638-8822>
 Anneliese Rillinger  <https://orcid.org/0000-0002-3091-8061>
 Jonathan J. Swift  <https://orcid.org/0000-0002-9486-818X>

References

- Akeson, R. L., Chen, X., Ciardi, D., et al. 2013, *PASP*, **125**, 989
 Allard, F., Homeier, D., & Freytag, B. 2012, *RSPTA*, **370**, 2765
 Astropy Collaboration, Price-Whelan, A. M., Sipőcz, B. M., et al. 2018, *AJ*, **156**, 123
 Astropy Collaboration, Robitaille, T. P., Tollerud, E. J., et al. 2013, *A&A*, **558**, A33
 Baraffe, I., Homeier, D., Allard, F., & Chabrier, G. 2015, *A&A*, **577**, A42
 Butters, O. W., West, R. G., Anderson, D. R., et al. 2010, *A&A*, **520**, L10
 Çakırlı, Ö. 2013, *NewA*, **22**, 15
 Çakırlı, Ö., İbanoğlu, C., & Sipahi, E. 2013, *NewA*, **20**, 1
 Chabrier, G. 2005, in *The Initial Mass Function 50 Years Later*, Vol. 327, ed. E. Corbelli, F. Palla, & H. Zinnecker (Dordrecht: Springer), 41
 Chabrier, G., Gallardo, J., & Baraffe, I. 2007, *A&A*, **472**, L17
 Claret, A. 1998, *A&A*, **335**, 647
 Cushing, M. C., Rayner, J. T., & Vacca, W. D. 2005, *ApJ*, **623**, 1115
 Dotter, A., Chaboyer, B., Jevremović, D., et al. 2008, *ApJS*, **178**, 89
 Eastman, J., Siverd, R., & Gaudi, B. S. 2010, *PASP*, **122**, 935
 Feiden, G. A., & Chaboyer, B. 2013, *ApJ*, **779**, 183
 Foreman-Mackey, D. 2016, *JOSS*, **1**, 24
 Foreman-Mackey, D., Hogg, D. W., Lang, D., & Goodman, J. 2013, *PASP*, **125**, 306
 Gillen, E., Hillenbrand, L. A., David, T. J., et al. 2017, *ApJ*, **849**, 11
 Han, E., Muirhead, P. S., Swift, J. J., et al. 2017, *AJ*, **154**, 100
 Iglesias-Marzoa, R., López-Morales, M., Arévalo, M. J., Coughlin, J. L., & Lázaro, C. 2017, *A&A*, **600**, A55
 Irwin, J. M., Quinn, S. N., Berta, Z. K., et al. 2011, *ApJ*, **742**, 123
 Kesseli, A. Y., Muirhead, P. S., Mann, A. W., & Mace, G. 2018, *AJ*, **155**, 225
 Kipping, D. M. 2013, *MNRAS*, **435**, 2152
 Kraus, A. L., Cody, A. M., Covey, K. R., et al. 2015, *ApJ*, **807**, 3
 MacDonald, J., & Mullan, D. J. 2017, *ApJ*, **850**, 58
 Markwardt, C. B. 2009, in *ASP Conf. Ser. 411, Astronomical Data Analysis Software and Systems XVIII*, ed. D. A. Bohlender, D. Durand, & P. Dowler (San Francisco, CA: ASP), 251
 O'Neill, K., Yin, Y., Edwards, N., & Swift, J. 2017, *AAS Meeting*, **229**, 155.03
 Park, C., Jaffe, D. T., Yuk, I.-S., et al. 2014, *Proc. SPIE*, **9147**, 91471D
 Parsons, S. G., Gänsicke, B. T., Marsh, T. R., et al. 2018, *MNRAS*, **481**, 1083
 Prato, L. A. 2017, *AAS Meeting*, **229**, 126.06
 Sim, C. K., Le, H. A. N., Pak, S., et al. 2014, *AdSpR*, **53**, 1647
 Swift, J., & Vyhnal, C. 2018, *RTSRE*, **1**, 281
 Torres, G., Andersen, J., & Giménez, A. 2010, *A&ARv*, **18**, 67
 Vacca, W. D., Cushing, M. C., & Rayner, J. T. 2003, *PASP*, **115**, 389
 Wright, J. T., & Eastman, J. D. 2014, *PASP*, **126**, 838
 Zucker, S., & Mazeh, T. 1994, *ApJ*, **420**, 806